Journal of Nuclear Medicine, published on August 31, 2023 as doi:10.2967/jnumed.123.265659

Total-Body Perfusion Imaging with [^{11}C]-Butanol

Elizabeth J. Li[1], Javier E. López[2], Benjamin A. Spencer[1], Yasser Abdelhafez[3], Ramsey D. Badawi[1,3], Guobao Wang[3], and Simon R. Cherry[1,3]

[1]*Department of Biomedical Engineering, UC Davis, Davis, California;* [2]*Department of Internal Medicine, Division of Cardiovascular Medicine, UC Davis Health, UC Davis, Sacramento, California; and* [3]*Department of Radiology, UC Davis Health, UC Davis, Sacramento, California*

Tissue perfusion can be affected by physiology or disease. With the advent of total-body PET, quantitative measurement of perfusion across the entire body is possible. [^{11}C]-butanol is a perfusion tracer with a superior extraction fraction compared with [^{15}O]-water and [^{13}N]-ammonia. To develop the methodology for total-body perfusion imaging, a pilot study using [^{11}C]-butanol on the uEXPLORER total-body PET/CT scanner was conducted. **Methods:** Eight participants (6 healthy volunteers and 2 patients with peripheral vascular disease [PVD]) were injected with a bolus of [^{11}C]-butanol and underwent 30-min dynamic acquisitions. Three healthy volunteers underwent repeat studies at rest (baseline) to assess test–retest reproducibility; 1 volunteer underwent paired rest and cold pressor test (CPT) studies. Changes in perfusion were measured in the paired rest–CPT study. For PVD patients, local changes in perfusion were investigated and correlated with patient medical history. Regional and parametric kinetic analysis methods were developed using a 1-tissue compartment model and leading-edge delay correction. **Results:** Estimated baseline perfusion values ranged from 0.02 to 1.95 $mL \cdot min^{-1} \cdot cm^{-3}$ across organs. Test–retest analysis showed that repeat baseline perfusion measurements were highly correlated (slope, 0.99; Pearson $r = 0.96$, $P < 0.001$). For the CPT subject, the largest regional increases were in skeletal muscle (psoas, 142%) and the myocardium (64%). One of the PVD patients showed increased collateral vessel growth in the calf because of a peripheral stenosis. Comorbidities including myocardial infarction, hypothyroidism, and renal failure were correlated with variations in organ-specific perfusion. **Conclusion:** This pilot study demonstrates the ability to obtain reproducible measurements of total-body perfusion using [^{11}C]-butanol. The methods are sensitive to local perturbations in flow because of physiologic stressors and disease.

Key Words: dynamic PET; kinetic modeling; perfusion and blood flow; [^{11}C]-butanol; total-body PET

J Nucl Med 2023; 00:1–8
DOI: 10.2967/jnumed.123.265659

Perfusion imaging using PET has been clinically used to assess single-organ, flow-related diseases such as cerebral stroke and myocardial ischemia (*1,2*). With the advent of total-body PET/CT, blood flow to all tissues in the body can be measured simultaneously, along with the image-derived input function (IDIF). This allows quantitative total-body perfusion measurements to be made with minimal invasiveness. Tissues of interest across the body have a range of perfusion values. However, commonly used tracers such as [^{15}O]-water, [^{82}Rb]-RbCl, and [^{13}N]-ammonia underestimate perfusion as flow increases because of their flow- and tissue-dependent extraction fraction (*3–5*). This is a challenge for measuring high flow rates, which can occur either inherently in some organs or in response to an external pressor, such as exercise, injection of adenosine, or increased partial pressure of CO_2 (*2,3,6*). Thus, accurate perfusion measurements require a highly extracted tracer that can be used to quantify perfusion over the range encountered in the human body in health and disease.

Butanol, labeled with ^{11}C or ^{15}O, has been used as a perfusion agent in both human (*3,7*) and preclinical (*8,9*) settings. It has the key advantage of having an approximately 100% extraction fraction in the brain for flows at least as high as 1.7 $mL \cdot min^{-1} \cdot g^{-1}$ (*4*). Furthermore, labeling with ^{11}C reduces positron range blurring relative to ^{15}O, ^{82}Rb, and ^{13}N (*10*) and, with its longer half-life, gives a wider time window to accommodate delays in administration. However, the metabolism- and tissue-dependent permeability of [^{11}C]-butanol presents challenges. [^{11}C]-butanol is metabolized in a manner similar to ethanol (*9*). Metabolism mainly occurs in the liver, where alcohol dehydrogenases break down [^{11}C]-butanol into [^{11}C]-butyric aldehyde and [^{11}C]-butyric acid, the latter of which can undergo β-oxidation to form [^{11}C]-CO_2 (*9*). Because these metabolites do not significantly affect the first-pass kinetics of [^{11}C]-butanol (*9*), it is possible to perform first-pass perfusion imaging of the entire body without the need for metabolite correction.

Because of the short acquisition time (AT), the improved sensitivity and extended axial field of view of total-body PET (*11*) are vital to multiorgan first-pass perfusion imaging with freely diffusible and reversible tracers such as [^{11}C]-butanol and [^{15}O]-water. In this work, we focused on developing a reliable methodology for quantifying perfusion across the body using kinetic modeling and demonstrating that these methods are sensitive to indications that alter perfusion. Baseline studies were conducted to establish the modeling approach and to determine quantitative perfusion values in a range of tissues. Reproducibility was assessed through resting test–retest studies. The sensitivity of the methods to changes in perfusion was assessed in 1 subject through a rest–stress paradigm generated via the cold pressor test (CPT) and by assessing regional ischemia and visualization of comorbidities in patients with peripheral vascular disease (PVD). These examples illustrate a few of the possible applications for total-body perfusion imaging. Although the short half-life of [^{11}C]-butanol may not be ideal for clinical use, it is an attractive tracer for systems-level physiologic research and studies of systemic chronic medical conditions such as heart, kidney, or liver failure. These methods can also be applied to studies with [^{15}O]-water.

Received Mar. 2, 2023; revision accepted Jul. 17, 2023.
For correspondence or reprints, contact Simon R. Cherry (srcherry@ucdavis.edu)
Published online Aug. 31, 2023.

MATERIALS AND METHODS

[^{11}C]-Butanol Synthesis

[^{11}C]-butanol was synthesized using an uninterrupted process beginning with radioactive [^{11}C]-CO_2, *n*-propyl magnesium chloride (Grignard solution) in ether, lithium aluminum hydride, and hydrochloric acid. The 20-min in situ process simultaneously purified [^{11}C]-butanol, formulated the final product solution, and sterilized and filtered the product solution into the vial after synthesis completion. Typical yields were 5,000 MBq (200–1,200 MBq/mL) at the end of synthesis, obtained from 60,000 MBq of [^{11}C]-CO_2. Radiochemical purity was in the range of 91%–97%.

Data Acquisition

With Institutional Review Board approval and written informed consent, 6 healthy volunteers (1 man, 5 women; body mass index, 20.9–30.4 kg/m^2; age, 23–64 y) and 2 patients with PVD (body mass index, 27.5 and 28.4 kg/m^2; 66-y-old man and 69-y-old woman, respectively) were imaged on the uEXPLORER PET/CT scanner (United Imaging Healthcare). A low-dose, total-body CT scan (140 kVp and 50 mAs with automatic dose modulation) was acquired for attenuation and scatter correction before bolus injection of [^{11}C]-butanol (mean, 281 MBq; range, 191–349 MBq). List-mode acquisitions on the uEXPLORER scanner (*11*) lasted about 30 min.

All 6 healthy volunteers received a baseline scan to measure resting perfusion across the body. One baseline visit from each of the 6 healthy volunteers (baseline healthy volunteers [BHVs]) was used to investigate total image-derived activity (TIDA) and optimize AT, as well as to report baseline perfusion values. Three healthy volunteers underwent a second baseline scan to assess test–retest reproducibility. One healthy volunteer underwent a paired resting and CPT study to measure effects of CPT. For subjects receiving 2 scans, visits occurred within 2 wk (9.0 ± 3.4 d). PVD patients had a single resting scan.

For the CPT, foot therapy pads (Polar Products) were placed on both feet before the CT acquisition. Starting after the CT scan but about 60 s before the start of the PET acquisition, ice water was continuously pumped through the conformable boots for 5 min.

Image Reconstruction

Reconstruction software, provided by the vendor, was used to perform time-of-flight ordered-subset expectation maximization (20 subsets and 4 iterations), with corrections for attenuation, scatter, randoms, dead time, and decay (*12*). No modeling of the point spread function or smoothing after reconstruction was applied. Images were reconstructed with 4.0 × 4.0 × 4.0 mm^3 voxels (matrix size, 150 × 150 × 486) and 57 frames (30 × 2, 12 × 5, 6 × 10, 4 × 30, and 5 × 300 s). The full 30-min dynamic reconstruction was used to measure TIDA and thus assess tracer metabolism. Only the first 5 min were used for kinetic modeling and perfusion estimation.

Region Delineation

Tissue time–activity curves were derived from 20 large or whole-organ volumetric regions of interest (ROIs) using PMOD software (PMOD Technologies), as listed in Supplemental Table 1 (supplemental materials are available at http://jnm.snmjournals.org). All bilateral regions were drawn separately (e.g., left and right kidneys) and averaged for kinetic modeling except for the deltoid, which demonstrated high spillover from the vessels in the arm in which the bolus was delivered; thus, only the contralateral deltoid was included. The CT scan was used for initial ROI delineation. ROIs were modified to account for the effects of subject motion in a tissue-dependent manner (Supplemental Table 1) through 2 image visualization strategies: use of a 0- to 5-min average PET image and avoidance of visible motion or spillover effects in high-contrast frames.

Volumetric ROIs were drawn in the descending aorta and the right ventricle (RV) to measure the IDIFs. For ROI-based time–activity curves, the descending aorta IDIF was used for all tissues except for the lungs, where the RV IDIF was used, because the dominant lung blood supply is via the pulmonary vein, not the bronchial artery (*13–15*). Parametric images were generated using the descending aorta IDIF for all voxels except for lung voxels, where the RV IDIF was used instead (supplemental materials, particularly Supplemental Fig. 1).

TIDA

Knapp et al. (*9*) found no metabolites in the blood during the first pass of [^{11}C]-butanol in a rabbit study. Because no blood sampling was performed in this study, TIDA curves for [^{11}C]-butanol were measured to assess end metabolism of [^{11}C]-butanol (characterized by expired [^{11}C]-CO_2 and loss of activity from the subject) during the first few minutes of acquisition used for kinetic modeling. Total-body PET can measure the total activity in the subject over time because the whole body is within the field of view. TIDA for each PET image frame m was defined as follows (*12*):

$$\mathrm{TIDA}(m) = V \times \sum\nolimits_i A_i(m), \qquad \text{Eq. 1}$$

where V is the voxel volume (mL) and $A_i(m)$ (MBq/mL) is the decay-corrected activity concentration of voxel i in frame m. For each study, TIDA(m) was normalized by injected dose. To account for timing variation of the bolus delivery, delay correction was performed on the TIDA curves using the leading-edge method (*16*), with a 1% threshold of the RV time–activity curve.

Kinetic Modeling

Three models were used in this work: a 0-tissue, 2-parameter model (v_b and delay); a 1-tissue, 4-parameter (1T4P) model (v_b, K_1, k_2, and delay); and a 1-tissue, 6-parameter (1T6P) model (v_b, K_1, k_2, delay, dispersion, and fraction contributed from a second blood input function) (*17*). v_b (mL·cm^{-3}) is the blood volume fraction, K_1 (mL·min^{-1}·cm^{-3}) represents perfusion, and k_2 (min^{-1}) represents the washout rate constant from the tissue back into systemic circulation. The partition coefficient p is K_1/k_2. After implementing leading-edge delay correction (*16*), modeling was performed using nonlinear least-squares fitting (*18*).

On the basis of preliminary fitting results and comparison of the Akaike information criterion for 1T4P and 1T6P models (with correction for small sample size), a 1T4P model was implemented for all ROI-based tissue time–activity curves except for the liver time–activity curve, for which the 1T6P model was used to account for the portal vein blood supply (Supplemental Table 2). No correction for lung tissue fraction was applied. Parameter identifiability and AT were investigated using these fixed models for ROI-based time–activity curves.

For parametric imaging, all 3 compartment models were considered for each voxel time–activity curve, where the 0-tissue, 2-parameter and 1T6P models were used to account for the blood pool and liver, respectively. Model selection was performed at the voxel level using the Akaike information criterion with correction for small sample size (supplemental materials).

AT

Because the Akaike information criterion depends on the number of image frames, we first compared the Akaike information criterion for each tissue with a constant AT of 180 s. After determining the most appropriate model based on an AT of 180 s, we explored how AT, or the delay-corrected total time of the time–activity curve used for kinetic modeling, affected the fitted parameters. Optimal AT was guided by the stability of the mean K_1, v_b, and p across ATs and the magnitude of the SD, as well as their relation to previously published literature values in Supplemental Table 3 (*3,6,13,14,19–43*). Time 0 was defined as the bolus arrival time in the ROI. ATs ranging from 60

to 270 s in 30-s increments were studied across all baseline acquisitions. For tissues that showed stability across ATs, 180 s was selected as the default.

Parameter Estimation

Using the appropriate model and AT, kinetic parameter estimates for ROI-based time–activity curves were obtained. Bilateral parameter estimates in the lungs and kidneys, as well as parameter estimates in most skeletal muscle regions (splenius capitis, psoas, thigh, and calf), were averaged to give a single value for each tissue. An identifiability analysis (*44–47*) for parameter identification also was performed (Supplemental Table 4).

For voxelwise kinetic modeling, image data were smoothed (*48*). An AT of 180 s was used with a leading-edge threshold of 7.5% to correct for delay (*16*) across all voxels. Further details are provided in the supplemental materials, particularly Supplemental Figure 2 and Supplemental Table 5.

Comparative Analysis

For the 3 BHV subjects with repeat scans, test–retest reproducibility was assessed first using Pearson *r*. A 1-sample Kolmogorov–Smirnov test was used to assess normality. After determining normality, Bland–Altman plots were generated with limits of agreement of 1.96 times the SD. A significance level of 0.05 was used. Additional test–retest assessments (the intraclass correlation coefficient and intrasubject coefficient of variation) are included in the supplemental materials.

For the rest–CPT study, intrasubject regional parameter estimates were compared. Assessments for the 2 PVD patients were made on the basis of clinical history and comorbidities.

RESULTS

IDIFs and ROI-based time–activity curves showed consistency in shape for a given tissue, whereas the magnitude varied across subjects (Fig. 1A). The time–activity curves of the 2 PVD subjects (Fig. 1A, red) were quite different in several tissues from those of the healthy subjects and were different from each other, indicating the heterogeneity of the perfusion patterns across disease states.

TIDA

As shown in Figure 1B, the normalized BHV TIDA curve decreased slowly over the course of the 30-min acquisition (~10% average drop overall), reflecting the expected loss of activity through the exhalation of [^{11}C]-CO_2. However, the curve remained quite flat over the first 5 min of the study (Fig. 1B, inset), confirming that metabolic losses of ^{11}C in the form of [^{11}C]-CO_2 are negligible for the ATs used for kinetic modeling and agreeing with previous measurements in animal studies (*9,49*). A small positive bias (<8%) was observed from 10 to 20 s—a previously noted effect that has been attributed to the injection of the bolus and small errors in correction factors with rapidly changing tracer distribution (*12*).

Impact of AT on Parameter Estimates

Figure 2 shows the stability of BHV estimates of K_1, v_b, and p as a function of the AT used for kinetic modeling for a subset of tissues. For most tissues, parameters were stable across ATs or reached stability by around 180–210 s after bolus arrival. A notable exception was the kidney, where K_1 was inversely related to p across ATs. Gray matter and skeletal muscle estimates of p were highly variable at shorter ATs but showed stabilization at longer ATs.

Using data similar to those in Figure 2, optimal ATs for all tissues were identified and fixed for each region for further analyses. All subsequent fitting at the ROI level was performed with the tissue-specific ATs listed in Table 1.

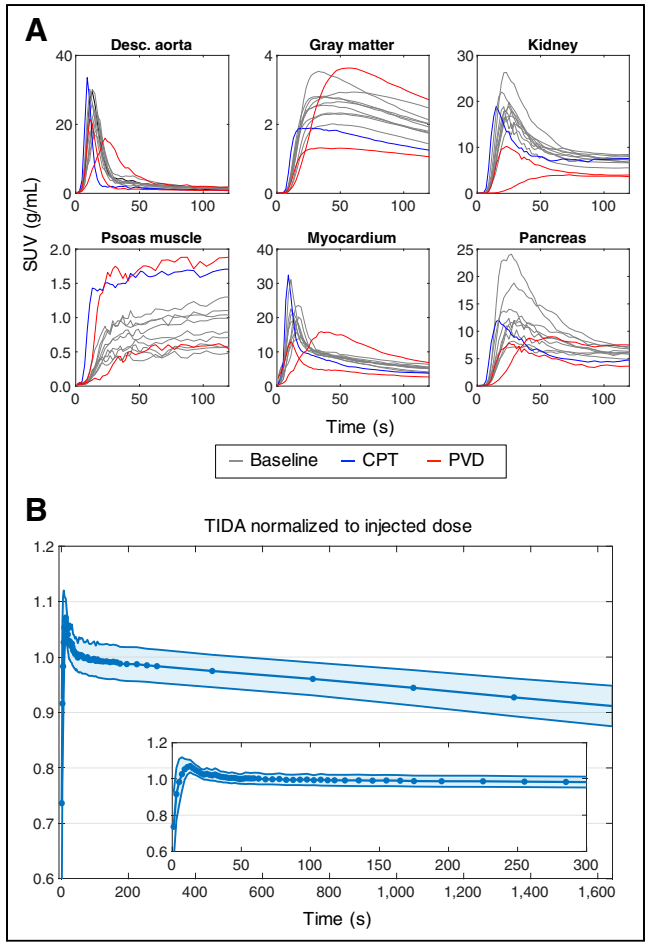

FIGURE 1. (A) Representative [^{11}C]-butanol time–activity curves (0–150 s) for subset of tissue types. (B) Normalized TIDA (mean ± SD) for BHV 30-min dynamic acquisitions. Desc. = descending.

Baseline Parameter Estimates in Healthy Volunteers

When the optimal AT was used (Table 1), all tissues except for the liver were fit with the 1T4P model, whereas the liver was fit with the 1T6P model (Supplemental Table 2). The leading-edge method failed to provide reasonable delay estimates for the liver; thus, delay correction in the liver was performed using joint estimation. The BHV results (Table 1, bold; Fig. 3) demonstrate the range of perfusion values (K_1) found across organs and tissues. One healthy subject showed abnormally low hepatic perfusion; after further investigation of the CT image, fatty infiltration of the liver was noted. Thus, the liver values for this subject were excluded from Table 1 and Figure 3. Tissue-specific BHV parameter estimates were compared with previously published literature values for individual organs (mostly obtained using [^{15}O]-water) as listed in Supplemental Table 3. Values were generally in good agreement, although direct comparison is difficult because of differences in the tracer used, modeling methodology, and imaging technology.

Test–Retest Assessments

Correlation analysis of the 3 test–retest subjects showed good agreement of K_1 (Fig. 4A; slope, 0.99; $r = 0.96$, $P < 0.001$), v_b (Fig. 4B; slope, 0.90; $r = 0.92$, $P < 0.001$), and delay (slope, 0.95; $r = 0.94$, $P < 0.001$) across all 16 tissue types, where the muscle regions were averaged. The partition coefficient p was also in agreement between visits (slope, 0.90; $r = 0.91$, $P < 0.001$). The Kolmogorov–Smirnov

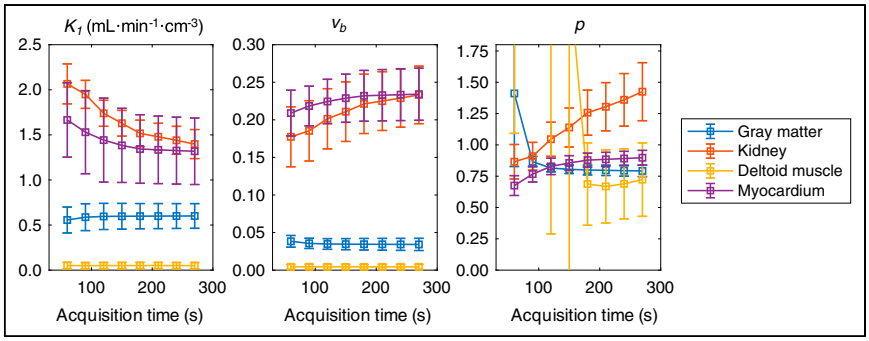

FIGURE 2. Impact of AT on BHV parameter estimates (mean ± SD) as assessed by fitting time–activity curves across ATs of 60–270 s in 30-s increments.

tests of the data showed a lack of normality, whereas the log-transformed data showed normality (Fig. 4). There were a range of intrasubject coefficient of variation and intraclass correlation coefficient values of K_1 across organs (Supplemental Table 6).

Parametric Imaging

The dynamic [^{11}C]-butanol data were of sufficient quality to produce low-noise parametric maps across the whole body. A representative baseline study is shown in Figure 5.

Effects of CPT

Compared with the corresponding resting scan, large increases in perfusion were observed after CPT in skeletal muscle, for which average K_1 increased from 0.06 to 0.14 mL·min^{-1}·cm^3. The overall range of K_1 after CPT was 0.07 mL·min^{-1}·cm^{-3} in the calves to 0.21 mL·min^{-1}·cm^{-3} in the deltoid. At rest, K_1 ranged from 0.04 mL·min^{-1}·cm^{-3} in the calves to 0.10 mL·min^{-1}·cm^{-3} in the deltoid. Regionally, the highest increase with CPT was in the psoas (142%), followed by the thigh muscles (137%), deltoid (111%), splenius capitis (106%), and calf muscles (71%). An increase in perfusion also was observed in the myocardium (rest, 1.48 mL·min^{-1}·cm^{-3}; CPT, 2.43 mL·min^{-1}·cm^{-3}). There was also a small increase in gray matter K_1 (rest, 0.47 mL·min^{-1}·cm^{-3}; CPT, 0.56 mL·min^{-1}·cm^{-3}). Thyroid perfusion showed a large decrease (rest, 1.64 mL·min^{-1}·cm^{-3}; CPT, 0.92 mL·min^{-1}·cm^{-3}). For the pancreas, spleen, and thyroid, v_b was lower for the CPT study. Regional differences from BHVs are shown in Supplemental Figure 3. There were also reductions in delay estimates of 1–3 s with CPT except for in the lungs, which showed the same delay estimate for both acquisitions.

These trends are visible in the parametric images (Fig. 6). Figure 6A shows changes in parametric K_1 images of the brain (increase in K_1 in gray matter and decrease in white matter). Short-axis, horizontal long-axis, and vertical long-axis views of the myocardium (Fig. 6B) and axial views of skeletal muscles in the thighs (Fig. 6C) show increased K_1.

PVD Patients

Results for the 2 PVD patients are shown in Figure 7. Patient 1 had a chronic and symptomatic left popliteal arterial stenosis and a prior myocardial infarction (Fig. 7A). Downstream of the popliteal stenosis, parametric assessment revealed an area of increased

TABLE 1
Tissue-Specific BHV Parameters (n = 6)

Category	Tissue	AT (s)	LE threshold (%)	Delay (s)	K_1	v_b	p
Brain	Gray matter	180	1.75	4.50 (0.84)	**0.60 (0.14)**	0.034 (0.008)	0.80 (0.04)
	White matter	180	2.00	4.67 (0.82)	**0.27 (0.05)**	0.016 (0.004)	0.65 (0.05)
Intestines	Large intestine	180	2.00	5.50 (2.74)	**0.11 (0.02)**	0.009 (0.008)	0.40 (0.11)
	Small intestine	180	2.00	7.00 (1.10)	**0.35 (0.06)**	0.039 (0.012)	1.18 (0.36)
Kidneys		90	1.50	4.92 (0.80)	**1.95 (0.16)**	0.185 (0.040)	0.91 (0.11)
Liver*		120	—	1.17 (1.33)	**1.23 (0.36)**	0.026 (0.054)	1.80 (0.43)
Lungs		60	2.50	3.50 (0.63)	**1.72 (0.32)**	0.089 (0.043)	0.16 (0.02)
Skeletal muscle†		240 (33)	3.56	8.50 (1.85)	**0.05 (0.02)**	0.003 (0.002)	1.71 (1.70)
Marrow and bone	Red marrow	180	2.00	2.17 (0.98)	**0.18 (0.07)**	0.009 (0.005)	0.67 (0.13)
	Trabecular bone	180	1.00	2.17 (2.56)	**0.02 (0.01)**	0.000 (0.001)	0.17 (0.13)
	Cortical bone	180	1.00	8.50 (3.94)	**0.03 (0.01)**	0.002 (0.002)	0.24 (0.12)
Myocardium		180	0.25	−3.17 (0.75)	**1.34 (0.38)**	0.232 (0.034)	0.88 (0.06)
Pancreas		120	3.00	5.00 (1.10)	**1.26 (0.60)**	0.096 (0.052)	0.93 (0.10)
Spleen		90	2.00	4.50 (0.55)	**1.65 (0.18)**	0.086 (0.028)	1.04 (0.03)
Stomach		120	5.00	4.17 (2.79)	**0.58 (0.15)**	0.028 (0.020)	0.81 (0.32)
Thyroid		180	3.00	5.00 (2.10)	**1.36 (0.34)**	0.220 (0.151)	0.78 (0.22)

*n = 5 (see text).
†Reported values are averaged.
LE = leading edge.
Data are mean followed by SD in parentheses. Units for K_1 are mL·min^{-1}·cm^{-3}.

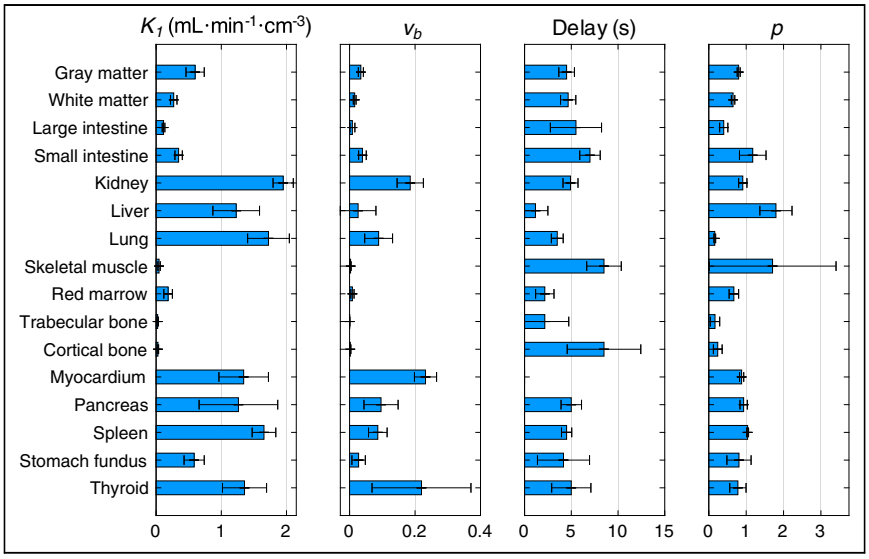

FIGURE 3. BHV ROI-based kinetic parameter estimates (mean ± SD). AT was fixed for individual tissues (Table 1).

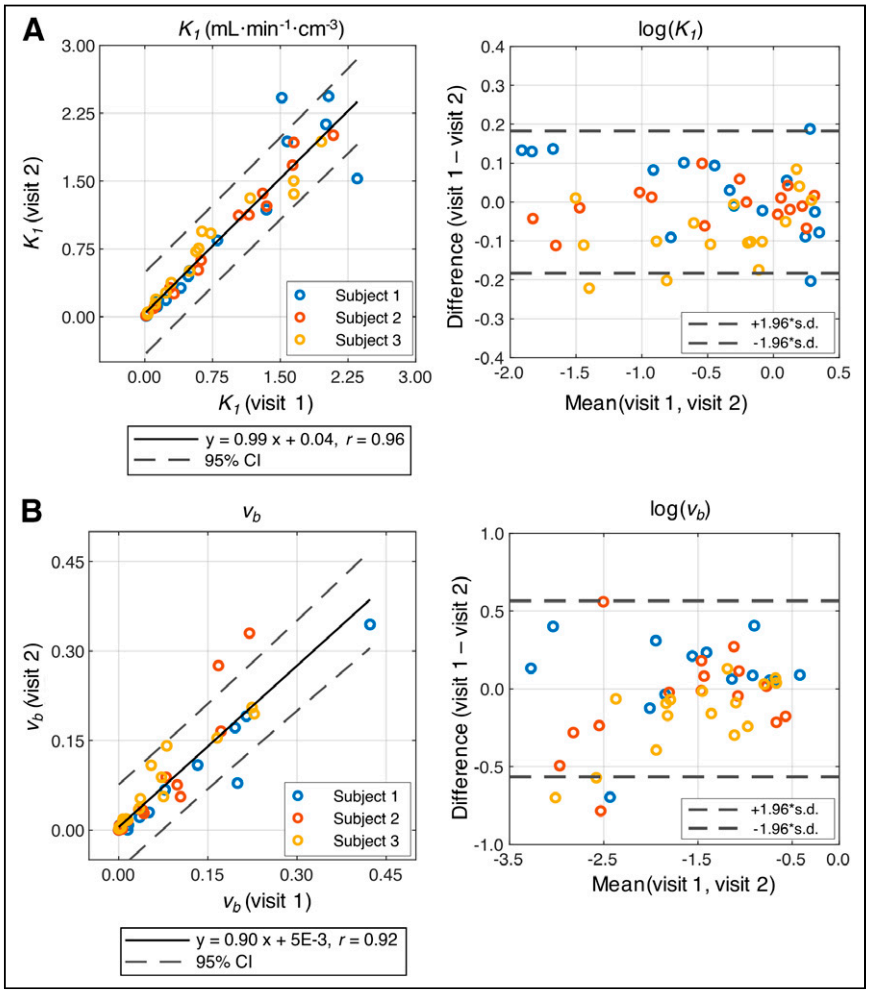

FIGURE 4. Correlation analysis and Bland–Altman plots of test–retest studies. K_1 (A) and v_b (B) showed strong agreement between 2 visits. Normality was observed for log-transformed data points shown in Bland–Altman plots for K_1 and v_b.

perfusion, with a 70% increase in K_1 relative to the right calf (0.074 vs. 0.044 mL·min^{-1}·cm^{-3}). Average skeletal muscle K_1 (0.11 mL·min^{-1}·cm^{-3}) was 146% higher than in BHV studies. Figure 7A includes myocardial short-axis, horizontal long-axis, and vertical long-axis parametric images. Whole myocardial perfusion for this PVD patient was 29% lower than BHV results (0.96 vs. 1.34 mL·min^{-1}·cm^{-3}).

The influence of known comorbidities—including renal failure, hypothyroidism, and right ventricular dilation—of PVD patient 2 were reflected in the parametric K_1 image (Fig. 7B) and the large regional differences compared with those of BHVs (Supplemental Fig. 4). In the kidney and thyroid, respectively, there were 85% and 71% reductions in K_1 compared with BHV studies (0.30 vs. 1.95 and 0.39 vs. 1.36 mL·min^{-1}·cm^{-3}). Patient 2 also had evidence of pulmonary hypertension in prior imaging studies (World Health Organization grade 2) and exhibited low lung K_1—with a dilated RV—compared with those of BHVs (94% drop; Supplemental Fig. 4).

DISCUSSION

We have presented methods and analyses for dynamic [^{11}C]-butanol total-body PET imaging to quantify tissue perfusion. An advantage of total-body PET is that perfusion and the tracer partition coefficient can be estimated simultaneously in every organ and tissue in the body (not possible with conventional scanners because of the fast kinetics of freely diffusible perfusion tracers). The high detection sensitivity of total-body PET allows high-quality, high-temporal-resolution (2-s frames) data to better capture the tissue time–activity curves and the input function, along with the potential for voxelwise kinetic modeling. Total ATs of approximately 5 min are sufficient for bolus delivery and capture of time–activity curves for all tissues and organs in the body, which then can be used to quantify perfusion using ROIs. An AT of 180 s from bolus arrival was suitable for most tissues. Average BHV parameter estimates were in broad agreement with single-organ literature values.

It is also possible to acquire whole-body perfusion images on conventional scanners with trapped perfusion tracers such as [^{13}N]-NH_3 and [^{62}Cu]-ethylglyoxal bis(thiosemicarbazonato)copper(II) (*43*). However, these tracers can have flow- or tissue-dependent extraction, which may make absolute quantification difficult

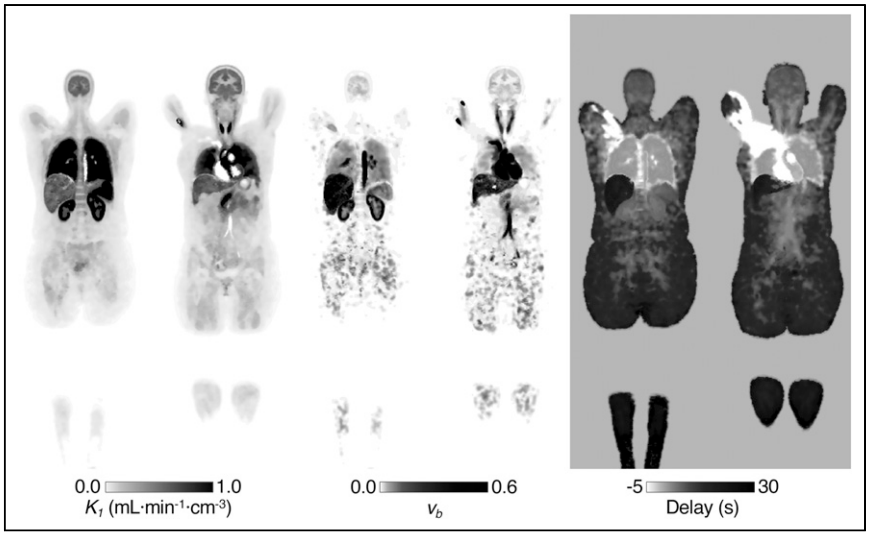

FIGURE 5. Example parametric images of 2 coronal slices (baseline). Grayscale bars have been manually adjusted to allow visualization across full range of values.

across all tissue types and blood flow ranges encountered in the body.

Baseline test–retest reproducibility in 3 healthy volunteers indicated that estimates of perfusion, v_b, and delay are all highly reproducible (Pearson $r > 0.9$, $P < 0.001$) between visits. The K_1 intrasubject coefficient of variation and intraclass correlation coefficient exhibited no clear pattern, although the kidney and spleen showed a particularly low intraclass correlation coefficient (<0) despite a high K_1. These highly perfused tissues may experience variable K_1 because of normal changes in function throughout the day (*50*) or stress-related effects linked to the imaging procedure. Estimates of p for the lung demonstrate that the RV IDIF and 1T4P model implemented in this work may not be sufficient to estimate lung perfusion and blood volume, because even with 2-s frames, lung v_b was underestimated relative to previously published values (Supplemental Table 3). Further investigation with a more complex model is likely necessary, as recently shown for [^{18}F]-FDG (*15*).

With CPT, a heterogeneous response across organs was observed as expected; previous studies have shown that flow increases in the myocardium (*51*), certain regions of the cerebral cortex (*52*), liver (*53*), and spleen (*54*), whereas blood flow decreases in the kidneys (*55*). To our knowledge, this is the first work to investigate changes in skeletal muscle blood flow with PET and CPT, especially across the entire body. CPT led to widespread changes in perfusion relative to rest (Fig. 6) and average BHV (Supplemental Fig. 3). Furthermore, delay estimates were shorter with CPT, indicative of an increased heart rate because of sympathetic nervous system stimulation. Although conclusions cannot be drawn from a single subject, the changes with CPT noted earlier are greater than the baseline test–retest range (Fig. 4). This demonstrates the sensitivity of total-body perfusion imaging with [^{11}C]-butanol in identifying multiorgan alterations in perfusion.

Similarly, larger changes in perfusion were observed in the PVD patients than in BHVs (Supplemental Fig. 4). PVD is a heterogeneous condition, typically affecting multiple organs and accompanied by other comorbidities. Both patients exhibited perfusion patterns that are consistent with their clinical symptoms and histories. These results highlight the potential utility of total-body perfusion imaging in assessing perfusion patterns across the entire body in systemic cardiovascular disease and support carefully designed imaging trials that can take advantage of this methodology.

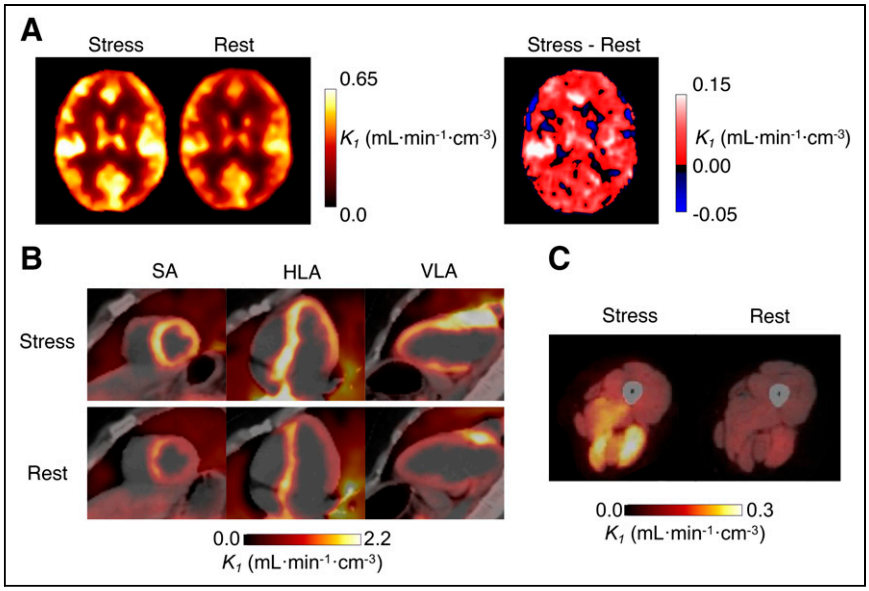

FIGURE 6. Intrasubject comparison between rest and stress (CPT) parametric images of K_1. Increases in gray matter (A), myocardial (B), and skeletal muscle (C) perfusion were observed with CPT, relative to rest. (B) Short-axis (SA), horizontal long-axis (HLA), and vertical long-axis (VLA) views show increased myocardial perfusion with CPT. (C) Similarly, axial cross section of thigh shows increased K_1 in specific muscle groups.

This study has several limitations. First, full testing and validation of TIDA as a surrogate for assessment of metabolism of [^{11}C]-butanol in humans is necessary through measurement of circulating metabolites, including [^{11}C]-CO_2 and [^{11}C]-bicarbonate. Second, [^{11}C]-butanol has not been extensively used outside research applications in the brain and myocardium. Direct comparison with [^{15}O]-water (for which our methods would also be applicable) would be helpful in other tissues to assess the effects of tissue-dependent permeability and the extent to which tissues known to metabolize alcohols (e.g., liver) or alcohol metabolites (e.g., muscle) need to be considered when using first-pass kinetic data to estimate perfusion. Third, the small positive TIDA bias present in early frames of the acquisition may affect the IDIF (and thereby introduce a small negative bias in K_1); thus, additional studies investigating this bias are warranted. However, given the

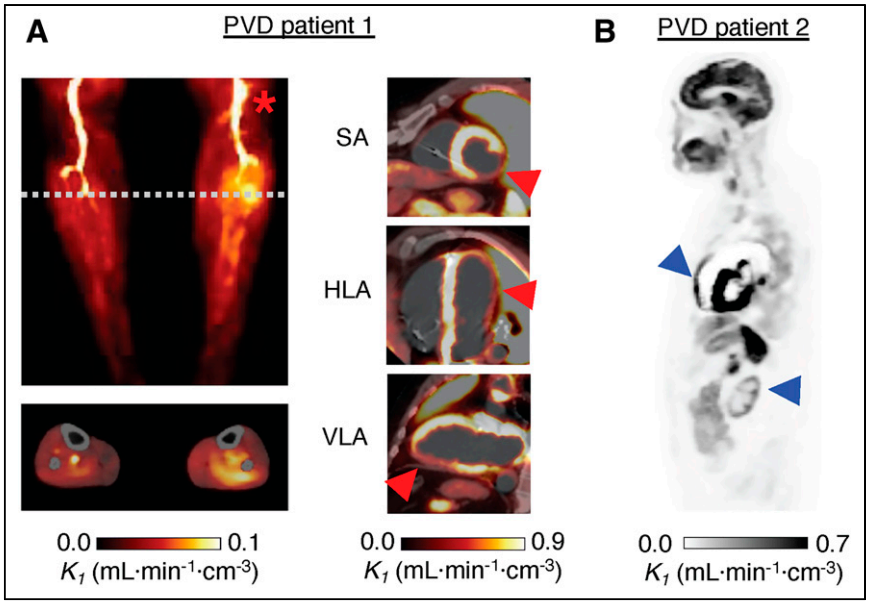

FIGURE 7. (A) Parametric K_1 images of PVD in patient 1. Maximum intensity projection showed increased perfusion in left calf, below popliteal occlusion (asterisk). Below, cross-sectional perfusion image was obtained at dashed line and overlayed on CT. Short-axis (SA), horizontal long-axis (HLA), and vertical long-axis (VLA) views show reduced perfusion at site of earlier myocardial infarction (arrowheads). (B) Perfusion image for PVD patient 2 showed several abnormalities—including enlarged RV and low renal cortex perfusion (arrowheads)—relative to BHVs (Table 1; Supplemental Fig. 4).

small magnitude and short duration of this bias, effects are not expected to be large, and similar effects are likely present in any dynamic PET acquisition with short image frames.

Fourth, because of the limited number of enrolled subjects, known heterogeneity of response to CPT challenges, and heterogeneous presentation of PVD, broader interpretations of perfusion differences or their significance are not possible. Fifth, although subjects abstained from caffeine 2 h before imaging, other factors may affect perfusion estimates—such as recent exercise, time of day, and stress imposed by the procedure—and thus may contribute to differences between scans. It is therefore likely that close attention to these factors could further improve test–retest reproducibility and reliability. Strategies to allow a pair of studies (baseline–intervention) to be performed in close succession (within 1 h) are being investigated.

Nonetheless, this work sets forth the methodology for dynamic total-body [^{11}C]-butanol imaging to quantify tissue perfusion. By providing measurements of baseline values in healthy volunteers, assessing test–retest reproducibility and reliability, and demonstrating changes in perfusion under a challenge (CPT) or with disease (PVD), this study lays the groundwork for application of total-body PET perfusion imaging in a range of physiologic research and in systemic cardiovascular diseases.

CONCLUSION

In this pilot study, we conducted total-body studies using [^{11}C]-butanol and developed analysis and kinetic modeling methodology for ROI-based measurement and parametric imaging of perfusion in all organs simultaneously. Reproducible measurements were obtained from tissues throughout the body. In addition, this work established that these methods were sensitive to changes in perfusion because of physiologic challenge and disease. This study sets the foundation for using total-body perfusion imaging with [^{11}C]-butanol in a range of physiologic research and in studying systemic cardiovascular disease.

KEY POINTS

QUESTION: Can [^{11}C]-butanol be used for the assessment of perfusion with total-body PET?

PERTINENT FINDINGS: Baseline perfusion measurements were reproducible, and these methods were sensitive to variations in perfusion because of physiologic perturbation and disease.

IMPLICATIONS FOR PATIENT CARE: Local changes and heterogeneity of flow across organs may be indications of disease. This study demonstrated that [^{11}C]-butanol can be used for quantitative assessment of perfusion through total-body PET, with potential application for systemic cardiovascular disease.

DISCLOSURE

This work was supported by NIH R01 CA206187 and R35 CA197608. UC Davis has a sales-based revenue-sharing agreement with United Imaging Healthcare. Ramsey Badawi and Simon Cherry are principal investigators on a research agreement with United Imaging Healthcare. No other potential conflict of interest relevant to this article was reported.

ACKNOWLEDGMENTS

We thank the EXPLORER team members, clinical research staff (particularly Lynda Painting), and technologists for their contributions to this work and Optimal Tracers for synthesizing [^{11}C]-butanol.

REFERENCES

1. Wang Z, Mascarenhas C, Jia X. Positron emission tomography after ischemic brain injury: current challenges and future developments. *Transl Stroke Res.* 2020;11:628–642.
2. Murthy VL, Bateman TM, Beanlands RS, et al. Clinical quantification of myocardial blood flow using PET: joint position paper of the SNMMI cardiovascular council and the ASNC. *J Nucl Cardiol.* 2018;25:269–297.
3. Berridge MS, Adler LP, Nelson AD, et al. Measurement of human cerebral blood flow with [^{15}O]-butanol and positron emission tomography. *J Cereb Blood Flow Metab.* 1991;11:707–715.
4. Herscovich P, Raichle ME, Kilbourne MR, Welch MJ. Positron emission tomographic measurement of cerebral blood flow and permeability–surface area product of water using [^{15}O]water and [^{11}C]butanol. *J Cereb Blood Flow Metab.* 1987;7:527–542.
5. Phelps ME, Huang SC, Hoffman EJ, Selin C, Kuhl DE. Cerebral extraction of N-13 ammonia: its dependence on cerebral blood flow and capillary permeability-surface area product. *Stroke.* 1981;12:607–619.
6. Quarles RP, Mintun MA, Larson KB, Markham J, Macleod AM, Raichle ME. Measurement of regional cerebral blood flow with positron emission tomography: a

comparison of [^{15}O]-water to [^{11}C]-butanol with distributed-parameter and compartmental models. *J Cereb Blood Flow Metab.* 1993;13:733–747.
7. Hack SN, Bergmann SR, Eichling JO, Sobel BE. Quantification of regional myocardial perfusion by exponential infusion of ^{11}C-butanol. *IEEE Trans Biomed Eng.* 1983;30:716–722.
8. Gjedde A, Hansen AJ, Siemkowicz E. Rapid simultaneous determination of regional blood flow and blood-brain glucose transfer in brain of rat. *Acta Physiol Scand.* 1980;108:321–330.
9. Knapp WH, Helus F, Oberdorfer F, et al. [^{11}C]-butanol for imaging of the blood-flow distribution in tumor-bearing animals. *Eur J Nucl Med.* 1985;10:540–548.
10. Sánchez-Crespo A, Andreo P, Larsson SA. Positron flight in human tissues and its influence on PET image spatial resolution. *Eur J Nucl Med Mol Imaging.* 2004;31:44–51.
11. Spencer BA, Berg E, Schmall JP, et al. Performance evaluation of the uEXPLORER total-body PET/CT scanner based on NEMA NU 2-2018 with additional tests to characterize PET scanners with a long axial field of view. *J Nucl Med.* 2021;62:861–870.
12. Leung EK, Berg E, Omidvari N, et al. Quantitative accuracy in total-body imaging using the uEXPLORER PET/CT scanner. *Phys Med Biol.* 2021;66:205008.
13. Schuster DP, Kaplan JD, Gauvain K, Welch MJ, Markham J. Measurement of regional pulmonary blood flow with PET. *J Nucl Med.* 1995;36:371–377.
14. Matsunaga K, Yanagawa M, Otsuka T, et al. Quantitative pulmonary blood flow measurement using ^{15}O-H_2O PET with and without tissue fraction correction: a comparison study. *EJNMMI Res.* 2017;7:102.
15. Wang Y, Spencer BA, Schmall J, et al. High-temporal-resolution lung kinetic modeling using total-body dynamic PET with time-delay and dispersion corrections. *J Nucl Med.* 2023;64:1154–1161.
16. Li EJ, Spencer BA, Schmall JP, et al. Efficient delay correction for total-body PET kinetic modeling using pulse timing methods. *J Nucl Med.* 2022;63:1266–1273.
17. Wang G, Corwin MT, Olson KA, Badawi RD, Sarkar S. Dynamic PET of human liver inflammation: impact of kinetic modeling with optimization-derived dual-blood input function. *Phys Med Biol.* 2018;63:155004.
18. Wang G, Qi J. Generalized algorithms for direct reconstruction of parametric images from dynamic PET data. *IEEE Trans Med Imaging.* 2009;28:1717–1726.
19. Leenders KL, Perani D, Lammertsma AA, et al. Cerebral blood flow, blood volume and oxygen utilization: normal values and effect of age. *Brain.* 1990;113:27–47.
20. Herzog H, Seitz RJ, Tellmann L, et al. Quantitation of regional cerebral blood flow with [^{15}O]-butanol and positron emission tomography in humans. *J Cereb Blood Flow Metab.* 1996;16:645–649.
21. Ito H, Kanno I, Iida H, et al. Arterial fraction of cerebral blood volume in humans measured by positron emission tomography. *Ann Nucl Med.* 2001;15:111–116.
22. Yamashita M, Inaba T, Oda Y, Mizukawa N. Renal blood volume vs. glomerular filtration rate: evaluation with [^{15}O]-CO and [^{88}Ga]-ethylenediaminetetraacetic acid (EDTA) study. *Radioisotopes.* 1989;38:373–376.
23. Kudomi N, Koivuviita N, Liukko KE, et al. Parametric renal blood flow imaging using [^{15}O]-H_2O and PET. *Eur J Nucl Med Mol Imaging.* 2009;36:683–691.
24. Taniguchi H, Masuyama M, Koyama H, Oguro A, Takahashi T. Quantitative measurement of human tissue hepatic blood volume by [^{15}O]-CO inhalation with positron-emission tomography. *Liver.* 1996;16:258–262.
25. Taniguchi H, Yamaguchi A, Kunishima S, et al. Using the spleen for time-delay correction of the input function in measuring hepatic blood flow with oxygen-15 water by dynamic PET. *Ann Nucl Med.* 1999;13:215–221.
26. Schober OH, Meyer GJ, Bossaller C, Creutzig H, Lichtlen PR, Hundeshagen H. Quantitative determination of regional extravascular lung water and regional blood volume in congestive heart failure. *Eur J Nucl Med.* 1985;10:17–24.
27. Brudin LH, Rhodes CG, Valind SO, Wollmer P, Hughes JMB. Regional lung density and blood volume in nonsmoking and smoking subjects measured by PET. *J Appl Physiol.* 1987;63:1324–1334.
28. Iida S, Harada Y, Ikenoue S, Moriya H. Measurement of bone marrow blood volume in the knee by positron emission tomography. *J Orthop Sci.* 1999;4:216–222.
29. Liu YJ, Yang HT, Yao MMS, et al. Quantifying lumbar vertebral perfusion by a Tofts model on DCE-MRI using segmental versus aortic arterial input function. *Sci Rep.* 2021;11:2920.
30. Martiat P, Ferrant A, Cogneau M, et al. Assessment of bone marrow blood flow using positron emission tomography: no relationship with bone marrow cellularity. *Br J Haematol.* 1987;66:307–310.
31. Kahn D, Weiner GJ, Ben-Haim S, et al. Positron emission tomographic measurement of bone marrow blood flow to the pelvis and lumbar vertebrae in young normal adults. *Blood.* 1994;83:958–963.
32. Raitakari M, Knuuti MJ, Ruotsalainen U, et al. Insulin increases blood volume in human skeletal muscle: studies using [^{15}O]CO and positron emission tomography. *Am J Physiol.* 1995;269:E1000-5.
33. Nuutila P, Raitakari M, Laine H, et al. Role of blood flow in regulating insulin-stimulated glucose uptake in humans: studies using bradykinin, [^{15}O]-water, and [^{18}F]-fluoro-deoxy-glucose and positron emission tomography. *J Clin Invest.* 1996;97:1741–1747.
34. Burchert W, Schellong S, Van Den Hoff J, Meyer GJ, Alexander K, Hundeshagen H. Oxygen-15-water PET assessment of muscular blood flow in peripheral vascular disease. *J Nucl Med.* 1997;38:93–98.
35. Iida H, Rhodes CG, De Silva R, et al. Myocardial tissue fraction correction for partial volume effects and measure of tissue viability. *J Nucl Med.* 1991;32:2169–2175.
36. Kaufmann PA, Gnecchi-Ruscone T, Yap JT, Rimoldi O, Camici PG. Assessment of the reproducibility of baseline and hyperemic myocardial blood flow measurements with [^{15}O]-labeled water and PET. *J Nucl Med.* 1999;40:1848–1856.
37. Delrue L, Blanckaert P, Mertens D, Van Meerbeeck S, Ceelen W, Duyck P. Tissue perfusion in pathologies of the pancreas: assessment using 128-slice computed tomography. *Abdom Imaging.* 2012;37:595–601.
38. Komar G, Kauhanen S, Liukko K, et al. Decreased blood flow with increased metabolic activity: a novel sign of pancreatic tumor aggressiveness. *Clin Cancer Res.* 2009;15:5511–5517.
39. Horsager J, Okkels N, Van Den Berge N, et al. In vivo vesicular acetylcholine transporter density in human peripheral organs: an [^{18}F]-FEOBV PET/CT study. *EJNMMI Res.* 2022;12:17.
40. Yan C, Han X, Liang X, Jia J, Xu Y, Zhao L. Non-invasive evaluation of esophageal varices in patients with liver cirrhosis using low-dose splenic perfusion CT. *Eur J Radiol.* 2022;152:110326.
41. Oguro A, Taniguchi H, Koyama H, et al. Quantification of human splenic blood flow (quantitative measurement of splenic blood flow with [^{15}O]-H_2O and a dynamic state method: 1). *Ann Nucl Med.* 1993;7:245–250.
42. Rumboldt Z, Al-Okaili R, Deveikis JP. Perfusion CT for head and neck tumors: pilot study. *AJNR.* 2005;26:1178–1185.
43. Fletcher JW, Logan TF, Eitel JA, et al. Whole-body PET/CT evaluation of tumor perfusion using generator-based [^{62}Cu]-ethylglyoxal bis(thiosemicarbazonato) copper(II): validation by direct comparison to [^{15}O]-water in metastatic renal cell carcinoma. *J Nucl Med.* 2015;56:56–62.
44. Mankoff DA, Shields AF, Graham MM, Link JM, Eary JF, Krohn KA. Kinetic analysis of 2-[^{11}C]-thymidine PET imaging studies: compartmental model and mathematical analysis. *J Nucl Med.* 1998;39:1043–1055.
45. Wells JM, Mankoff DA, Muzi M, et al. Kinetic analysis of 2-[^{11}C]-thymidine PET imaging studies of malignant brain tumors: compartmental model investigation and mathematical analysis. *Mol Imaging.* 2002;1:151–159.
46. Muzi M, Mankoff DA, Grierson JR, Wells JM, Vesselle H, Krohn KA. Kinetic modeling of 3′-deoxy-3′-fluorothymidine in somatic tumors: mathematical studies. *J Nucl Med.* 2005;46:371–380.
47. Zuo Y, Sarkar S, Corwin MT, Olson K, Badawi RD, Wang G. Structural and practical identifiability of dual-input kinetic modeling in dynamic PET of liver inflammation. *Phys Med Biol.* 2019;64:175023.
48. Wang G, Nardo L, Parikh M, et al. Total-body PET multiparametric imaging of cancer using a voxelwise strategy of compartmental modeling. *J Nucl Med.* 2022;63:1274–1281.
49. DiVincenzo GD, Hamilton ML. Fate of n-butanol in rats after oral administration and its uptake by dogs after inhalation or skin application. *Toxicol Appl Pharmacol.* 1979;48:317–325.
50. Dibner C, Schibler U. Circadian timing of metabolism in animal models and humans. *J Intern Med.* 2015;277:513–527.
51. Schindler TH, Nitzsche EU, Olschewski M, et al. PET-measured responses of MBF to cold pressor testing correlate with indices of coronary vasomotion on quantitative coronary angiography. *J Nucl Med.* 2004;45:419–428.
52. Petrovic P, Petersson KM, Ghatan PH, Stone-Elander S, Ingvar M. Pain-related cerebral activation is altered by a distracting cognitive task. *Pain.* 2000;85:19–30.
53. Keramida G, Gregg S, Peters AM. Stimulation of the hepatic arterial buffer response using exogenous adenosine: hepatic rest/stress perfusion imaging. *Eur Radiol.* 2020;30:5852–5861.
54. Galea N, Cundari G, Borrazzo C, et al. Splenic blood flow increases after hypothermic stimulus (cold pressor test): a perfusion magnetic resonance study. *BioMed Res Int.* 2019;2019:8437927.
55. Kannenkeril D, Janka R, Bosch A, et al. Detection of changes in renal blood flow using arterial spin labeling MRI. *Am J Nephrol.* 2021;52:69–75.